




# Optimization of biocorrosion resistance and mechanical properties of PM Ti–XAl–2Fe–3Cu alloys by response surface methodology

Mojtaba Najafizadeh<sup>1</sup>, Mehran Ghasempour-Mouziraji<sup>2,3</sup>, Morteza Hosseinzadeh<sup>4</sup>, Sahar Yazdi<sup>5</sup>, Ahmadreza Sarrafan<sup>6</sup>, Mansoor Bozorg<sup>7,\*</sup>, Pasquale Cavaliere<sup>8,\*</sup> , Aleksandra Laska<sup>9</sup>, and Marek Szkodo<sup>9</sup>

<sup>1</sup>The State Key Laboratory of Metal Matrix Composites, School of Materials Science and Engineering, Shanghai Jiao Tong University, Shanghai 200240, China

<sup>2</sup>TEMA - Centre for Mechanical Technology and Automation, University of Aveiro, Aveiro, Portugal

<sup>3</sup>EMaRT Group, School of Design, Management and Production Technologies, University of Aveiro, Estrada do Cercal 449, 3720-509 Oliveira de Azeméis, Portugal

<sup>4</sup>Department of Mechanical Engineering, Ayatolla Amoli Branch-Islamic Azad University, Amol, Iran

<sup>5</sup>School of Medical Sciences, Shahrood Branch, Islamic Azad University, Shahrood, Iran

<sup>6</sup>Babol University of Medical Science, Mazandaran, Iran

<sup>7</sup>Department of Chemical and Materials Engineering, Shahrood University of Technology, Shahrood 3619995161, Iran

<sup>8</sup>Department of Innovation Engineering, University of Salento, Via per Arnesano, 73100 Lecce, Italy

<sup>9</sup>Faculty of Mechanical Engineering and Ship Technology, Gdansk University of Technology, Narutowicza 11/12, 80-233 Gdansk, Poland

Received: 15 June 2022

Accepted: 19 September 2022

© The Author(s) 2022

## ABSTRACT

In the current study, the biocorrosion resistance and mechanical properties of the Ti–XAl–2Fe–3Cu (wt%) ( $X = 6, 4, 2$  wt%) alloy produced by powder compact extrusion of blended elemental powders were optimized by using the response surface methodology in order to gain the best combination of processing parameters. To run the optimization process, central composite design with three equal levels of oxygen, hydrogen and aluminum was used and, by employing ANOVA, the analysis of variance was implemented. The results showed that the content of aluminum has a significant effect on the microstructure, mechanical properties, biocorrosion resistance and fracture behavior of the extruded rods. The highest aluminum content corresponds to the highest alloy strength and biocorrosion resistance. This was due to the reduction of the lamella thickness and of the material colonies as the aluminum content increases. Also, by running the experimental and optimization tests, the

Handling Editor: Catalin Croitoru.

Address correspondence to E-mail: bozorg.mansoor@gmail.com; pasquale.cavaliere@unisalento.it  
E-mail Addresses: mojtaba@sjtu.edu.cn; mehran@ua.pt; m\_hoseinzadeh59@yahoo.com; sahar yazdi70@yahoo.com; Ahmadrezasarrafan5960@gmail.com; aleksandra.laska@pg.edu.pl; mszkodo@pg.edu.pl

<https://doi.org/10.1007/s10853-022-07768-7>

Published online: 08 October 2022

mechanical properties resulted 1245 MPa in yield strength and 1340 MPa in ultimate tensile strength with  $0.1 \mu\text{Acm}^{-2}$  in corrosion current.

## Introduction

Titanium and its alloys are broadly used in different applications in the biomedical field such as orthopedic and dental implants due to their light weight, high corrosion resistance and low elastic modulus as compared with the other metallic biomaterials such as stainless steels and Co–Cr–based alloys [1–3]. Recently, in the dental field both low- and high-strength titanium alloys have been introduced [4, 5]. Anyway, the low-strength and high-strength titanium and its alloys have several disadvantages.

For the low strength, polishing is too difficult and poor wear resistance causes limitations in the high-stress conditions; the higher elastic modulus of high-strength titanium alloys has the higher effect on shielding stress between implant and bone for surgically implant parts [4, 6, 7].

Recently, we have fabricated a Ti–2.7Al–3Cu–2Fe (wt%) alloy by hot extrusion of a compact of TiH<sub>2</sub>, Al, Fe and Cu powder blend, and demonstrated that the alloy has a fully  $\alpha/\beta$  lamellar microstructure with a high yield strength (YS) of 1072 MPa, high ultimate tensile strength (UTS) of 1220 MPa and a relatively low tensile ductility of 2.7% [8]. It was also shown that this alloy has a great potential for biomedical applications due to its high corrosion resistance [9]. Furthermore, the high-strength titanium alloys such as Ti–6Al–4V with the releasing of V ions from the wear corrosion and passive film dissolution on the alloy surface have a toxic effect for the long-term performance, since high condensation of V ions in the blood causes health problems [10, 11]. Recently, the design trend moved to new biomedical titanium alloys through reducing elastic modulus and controlling the addition of toxic alloying elements [12–14].

Products belonging to cellular metabolism (as hydrogen peroxide, or bacterial products) tend to influence the corrosion behavior of titanium plants. These are absorbed on surfaces modifying the corrosion behavior and leading to the formation of further chemical species. In addition, cells and bacteria can act as biofilm producers contributing to influence

the corrosion resistance of the plants. These features can be amplified once tribocorrosion or fretting corrosion takes place locally. So, in all these conditions, the corrosion/dissolution behavior of biomedical titanium alloys must be carefully analyzed.

To improve mechanical properties, corrosion resistance, high-temperature properties and formability of titanium, different alloying elements must be added [14–16]. A safe alloying element to improve the properties of titanium alloys to be applied in the biomedical field is Fe leading to low elastic modulus, high-strength, non-toxic, non-allergic and low-cost alloys [17]. The addition of copper to titanium can improve antibacterial properties. Antibacterial capability is dependent on the Cu content; for percentage lower than 5 wt %, antibacterial and mechanical properties are improved [18, 19]. The industries more likely accept the addition of Fe because of its low cost and the improvement of mechanical properties of Ti alloys by adding Fe [8, 20]. Fe is a  $\beta$ -eutectic, non-toxic and non-allergic element [8], and with an addition of 1–4 wt.% Fe to the Ti alloys, good mechanical properties can be obtained [9]. Besides what has been mentioned, various researches have been done in the direction of the optimization of the production process. Najafizade et al. [21] optimized siliconizing performance by using RSM method and experimental tests. Hoseinzade et al. [22] optimized the tube drawing performance with rectangular tubes to optimize the friction coefficient, drawing velocity, bearing length and die half angle. New developments in science and technology have significant impact on human health and life [23–27]. Since the mechanical properties of Ti alloys are important for the application in the biomedical field, in this paper, we tried to find the optimal combination of process parameters to have the best mechanical and microstructural properties that have not been carried out in the previous researches [28–30]. So, lack of this issue was the key motivation of this research. Based on the literature, there has not been a comprehensive study on the optimization of mechanical and biocorrosion properties of Ti alloys. This motivated the authors to carry out a research in this field.

The aim of the present paper is the optimization of the composition and processing parameters of a new developed Ti-XAl-2Fe-3Cu alloy in order to improve the mechanical properties and the biocorrosion behavior.

## Experimental

### Specimens preparation

Ti-Al-Fe-Cu alloy rods were fabricated by extruding a compact of a mixture of TiH<sub>2</sub>, Al, Fe and Cu powders, with a composition of Ti-2Fe-3Cu-XAl ( $X = 6, 4, 2$  wt%), at 1200 °C and with 5 min of holding time. A hydraulic press with 200-ton capacity was employed. The purity and particle size of TiH<sub>2</sub> powder were 99.5% and 75 μm (– 200 mesh), respectively. Al powder with particle sizes 40 μm (– 325 mesh), Cu powder of 40 μm (– 325 mesh) and Fe powder with particle sizes smaller than 53 μm (– 300 mesh) produced via gas atomization were employed. In order to reduce the moisture levels, all powders were heated in a vacuum oven for 2 h at 100 °C; tumbler mixing for 24 h was employed for the blending.

The powder mixture was then cold-pressed to produce cylindrical powder compacts with a relative density of around 85%. The powder compact was heated to 1200 °C by induction heating in an argon atmosphere with oxygen content below 200 ppm, held at this temperature for 5 min and then left to be cooled down at room temperature. The extrusion cylinder and stainless-steel die were heated to 500 °C before the extrusion process. The extrusion ratio was 9:1 in order to produce cylindrical rods of 100 mm in diameter. The overall schematic of the process is shown in Figs. 1a, b.

The oxygen and hydrogen contents of the extruded rods were measured by using a LECO TCH-600 nitrogen/oxygen/hydrogen analyzer, as shown in Table 1. A Rigaku Ultima IV XRD was used to identify the phase structure of the extruded rods by applying Cu-K $\alpha$  radiation at a precipitating voltage of 40 kV and a current of 40 mA with a scan step of 0.02. The microstructure of the as-extruded rods was characterized by using an OLYMPUS BX51M optical microscopy and FEI NOVA NanoSEM 230 scanning electron microscope. The cross sections of the extruded rods were polished with traditional metallographic techniques and etched with Kroll solution

(2 ml HF, 6 ml HNO<sub>3</sub>, 92 ml H<sub>2</sub>O) for preparing them for microstructural analysis by optical microscopy. To check and recognize the average sizes of different phases in alloys, DT2000 software was used. The tensile test specimens with a gauge length of 15 mm and a thickness of 2 mm and a width of 3 mm were cut along the extrusion direction using an electrical discharge wire machine. The tensile tests were performed by using a Zwick/Roll Z20 universal testing machine at room temperature. The strain was measured by using an extensometer with a gauge length of 12 mm. The strain rate of the tests was set at  $5 \times 10^{-4} \text{ s}^{-1}$ . The fracture surfaces and the longitudinal cross section near the fracture of the tensile test specimens were examined using SEM.

### Electrochemical test

Electrochemical measurements were performed by using a biologic vsp-300 potentiostat. In a conventional three-electrode cell configuration, Ti-Al-Cu-Fe samples were used as the working electrode, platinum electrode as the counter electrode (CE) and saturated calomel electrode (SCE), separated from the cell by a glass frit, as the reference electrode (RE). It is worth noting that all the reported potential in this text refers to SCE and the electrochemical cell was open to the air. The immersion time for electrochemical measurements was 1 h at 298 K. Electrochemical impedance spectroscopy (EIS) was performed with the frequency ranging from 100 kHz to 10 mHz at open-circuit potential. The sinusoidal potential perturbation was 5 mV in amplitude. Polarization tests were performed from – 250 mV to + 2 V around the OCP with a scan rate of 1 mV/s.

## Result and discussion

### Optimization

#### *Creation of the design matrix with response surface methodology (RSM)*

Needless to say, having the best combination of process parameters would be highly beneficial for both industrial and academic purposes. To do so, in the current research, hydrogen, oxygen and Al percentage were considered to reach this aim. In addition, the four output parameters, namely elongation,

**Figure 1** a Flowchart of the experimental procedure and b Schematic diagram of the experimental setup.

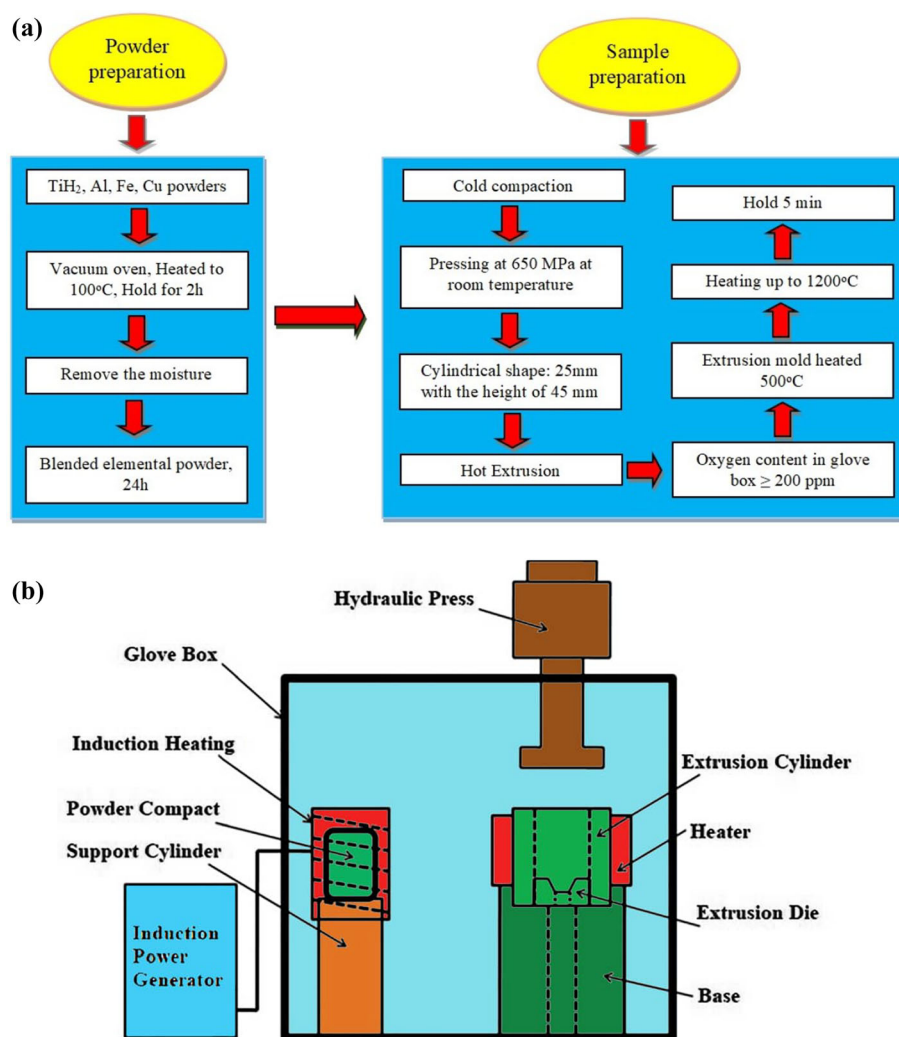


**Table 1** Level of process parameters

Factors	Symbol	Unit	Level 1	Level 2	Level 3
Oxygen	<i>O</i>	Wt%	0.3	0.31	0.32
Hydrogen	<i>H</i>	Wt%	0.11	0.12	0.13
Al	<i>Al</i>	Wt%	2	4	6

UTS,  $YS$  and  $I_{corr}$  were considered as fundamental to fulfill the optimization process. RSM is a method that combines mathematical and statistical evaluation of a model in order to analyze a specific process. The outputs (responses) are influenced by input parameters and the main goal of this method is to optimize or to find the optimal combination of process parameters based on the desired boundary conditions. RSM consists of two main models that are widely used in the studies and projects, namely CCD

(central composite design) and Box–Behnken. The main difference between these two models is the range of selection for input parameters. The most important feature of RSM is DOE (design of experiment) which tries to find the most suitable point in which the outputs are examined.

Having determined the inputs and outputs, central composite design (CCD) approach was applied to run optimization. In the RSM approach, the values need to be sorted as the lowest, middle and highest value. In the RSM, the minimum, middle and maximum values are considered as  $(-1)$ ,  $(0)$  and  $(1)$ , respectively, and the alpha value has been considered as 1 in the optimization. It is worth noting that the key reason to run optimization is reducing the cost and time in the experimental test. The mentioned parameters and their considered ranges are shown in Table 1. For running test and achieving the results, a

design matrix (Table 1) was set and the results are reported in Table 2.

In this stage and after collecting all data, the empirical equations for outputs are obtained. The empirical equations provide information about the relationships between outputs and process parameters.

$$\begin{aligned} \text{Elongation} = & 2.080. - 2700 A - 0.1600 B - 0.6600 C \\ & + 0.1125 + AB + 0.0375 AC \\ & + 0.0125 BC - 0.0591 A - 0.1091 B \\ & + 0.2909 C \end{aligned} \tag{1}$$

$$\begin{aligned} \text{UTS} = & +1231.98 + 13.90 A + 8.40 B + 33.00 C \\ & - 6.00 AB - 2.25 AC - 4.25 BC + 2.05 A \\ & - 0.4545 B + 29.55 C \end{aligned} \tag{2}$$

$$\text{YS} = +1152.10 + 11.20 A + 5.90 B + 71.90 C \tag{3}$$

$$I_{\text{corr}} = +0.1275 + 0.0000 A + 0.0000 B - 0.0250 C \tag{4}$$

The above-mentioned Eqs. (1–4) were used to check the rate of accuracy of the models and to do this checking, ANOVA was used. Having checked the results and p values of the achieved results, the corresponding graphs are extracted. Table 3 (a, b, c, d) shows the analysis of the variance calculated through ANOVA for the outputs needed in the current research.

Figure 2 (a–d) indicates the input parameters and their effects on the respective outputs.

*Effect of process parameters on UTS*

Figure 3 shows the effect of the oxygen, hydrogen and aluminum content on the ultimate tensile strength (UTS). As can be seen from Fig. 3a, with the increase in the oxygen and hydrogen percentages in the alloy the UTS is slightly increased. On the other hand, Fig. 3b, c shows the combined effect of Al with O and H, respectively. With the increase in the percentage of the Al and O, the UTS significantly increased, as compared to the oxygen and hydrogen shown in Fig. 3a. Al content has a strong effect on the UTS because Al is  $\alpha$  phase stabilizer in titanium alloys. With the increase in Al percentage, the  $\alpha$  phase percentage increases in the Ti alloys. Anyway, the presence of a higher percentage of  $\alpha$  phase inside the Ti alloys leads to brittleness as it will be shown in the analysis of elongation to failure of these alloys.

*Effect of process parameters on YS*

Figure 4 shows the effect of the different alloying elements on yield stress (YS) of the Ti–XAl–2Fe–3Cu alloy. The main elements affecting the YS behavior are oxygen, hydrogen and aluminum. As can be seen

**Table 2** Design matrix and outputs

Run	A:Hydrogen	B:Oxygen	C:Al	Elongation	UTS	YS	$I_{\text{corr}}$
1	0.13	0.3	2	2.5	1220	1103	0.15
2	0.12	0.31	4	2	1240	1159	0.13
3	0.12	0.3	4	2.2	1230	1141	0.13
4	0.12	0.32	4	1.9	1226	1142	0.13
5	0.12	0.31	4	2.2	1222	1141	0.13
6	0.12	0.31	6	1.7	1292	1223	0.1
7	0.13	0.31	4	1.9	1226	1142	0.13
8	0.11	0.31	4	2.3	1227	1146	0.13
9	0.11	0.3	6	2	1278	1209	0.1
10	0.12	0.31	2	3.2	1216	1064	0.15
11	0.12	0.31	4	2	1240	1159	0.13
12	0.12	0.31	4	2	1240	1159	0.13
13	0.11	0.3	2	3.5	1185	1052	0.15
14	0.12	0.31	4	2	1240	1159	0.13
15	0.13	0.3	6	1.4	1304	1231	0.1
16	0.13	0.32	6	1.2	1320	1245	0.1
17	0.11	0.32	2	2.8	1230	1086	0.15
18	0.12	0.31	4	2	1240	1159	0.13
19	0.11	0.32	6	1.6	1285	1219	0.1
20	0.13	0.32	2	2.5	1220	1103	0.15



**Table 3** Variance calculations for the analysed outputs. The data belong directly from the software ANOVA

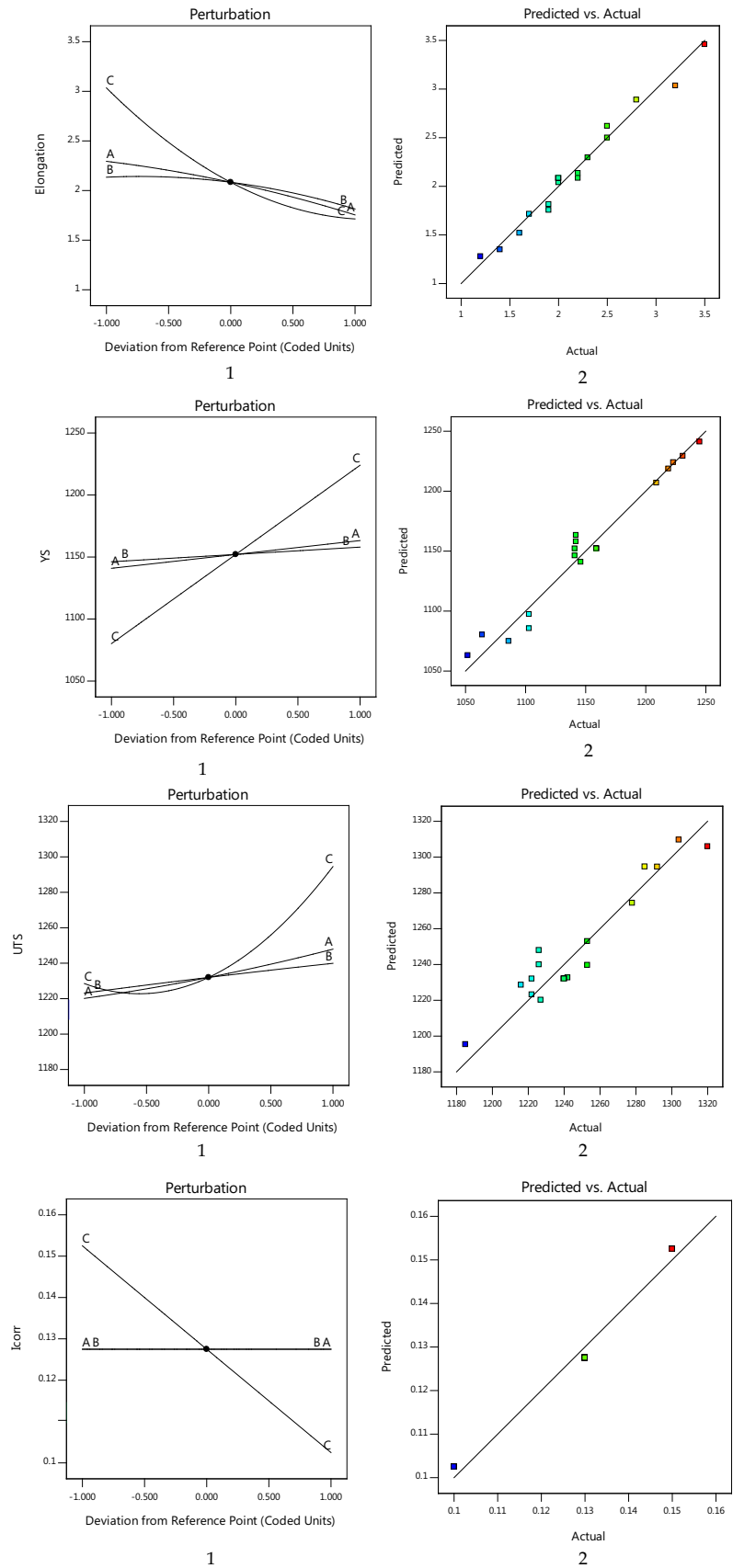
Source	Sum of squares	df	Mean square	F value	p value	Significant
<i>(a) Analysis of variance for UTS</i>						
Model	18663.77	9	2073.75	10.28	0.0006	
A—Hydrogen	1932.10	1	1932.10	9.58	0.0113	
B—Oxygen	705.60	1	705.60	3.50	0.0910	
C—Al	10890.00	1	10,890.00	53.99	< 0.0001	
AB	288.00	1	288.00	1.43	0.2597	
AC	40.50	1	40.50	0.2008	0.6636	
BC	144.50	1	144.50	0.7163	0.4171	
A <sup>2</sup>	11.51	1	11.51	0.0570	0.8161	
B <sup>2</sup>	0.5682	1	0.5682	0.0028	0.9587	
C <sup>2</sup>	2400.57	1	2400.57	11.90	0.0062	
<i>(b) Analysis of variance for elongation</i>						
Model	5.70	9	0.6333	42.36	< 0.0001	
A—Hydrogen	0.7290	1	0.7290	48.76	< 0.0001	
B—Oxygen	0.2560	1	0.2560	17.12	0.0020	
C—Al	4.36	1	4.36	291.33	< 0.0001	
AB	0.1013	1	0.1013	6.77	0.0264	
AC	0.0112	1	0.0112	0.7524	0.4061	
BC	0.0012	1	0.0012	0.0836	0.7784	
A <sup>2</sup>	0.0096	1	0.0096	0.6422	0.4415	
B <sup>2</sup>	0.0327	1	0.0327	2.19	0.1698	
C <sup>2</sup>	0.2327	1	0.2327	15.56	0.0028	
<i>(c) Analysis of variance for YS</i>						
Model	53,298.60	3	17766.20	142.47	< 0.0001	
A—Hydrogen	1254.40	1	1254.40	10.06	0.0059	
B—Oxygen	348.10	1	348.10	2.79	0.1142	
C—Al	51,696.10	1	51696.10	414.56	< 0.0001	
<i>(d) Analysis of variance for I<sub>corr</sub></i>						
Model	0.0062	3	0.0021	266.67	< 0.0001	
A—Hydrogen	0.0000	1	0.0000	0.0000	1.0000	
B—Oxygen	0.0000	1	0.0000	0.0000	1.0000	
C—Al	0.0062	1	0.0062	800.00	< 0.0001	
Residual	0.0001	16	7.813E-06			
Lack of fit	0.0001	11	0.0000			
Pure error	0.0000	5	0.0000			
Cor total	0.0064	19				

from Fig. 4a, with the increase in the oxygen and hydrogen percentage the YS is marginally increased. The main reason for this phenomenon is due to the fact that O is  $\alpha$  stabilizer and H is  $\beta$  stabilizer. However, both oxygen and hydrogen increase the brittleness of this kind of alloys. With the increase in oxygen, the  $\alpha$  phase grows inside the Ti alloys, this leads to increase in the yield stress. Figure 4b shows the effect of H and Al content on the YS of the alloys. By enhancing H and Al percentage, the YS increased. As Al is a strong  $\alpha$  stabilizer, the most efficient way to increase YS if the increasing of aluminum content.

### Effect of process parameters on Elongation

Figure 5 shows the effect of all the alloying elements on the elongation to failure of the Ti-XAl-2Fe-3Cu alloy. As can be seen from Fig. 5a, the elongation increased with the decrease in the O and H contents. Oxygen is an  $\alpha$  stabilizer and with the increase in O and H in the titanium alloys, the TiO<sub>2</sub> and TiH<sub>2</sub> intermetallics percentages increase [20]. The development of these intermetallics leads to a decrease in the elongation to failure. Figures 5b, c shows how elongation to failure decreases as the aluminum

**Figure 2 a–d** input parameters variations and their effects on the outputs (the left pictures indicate the variation, the right pictures indicate the comparison between the measured and predicted data).



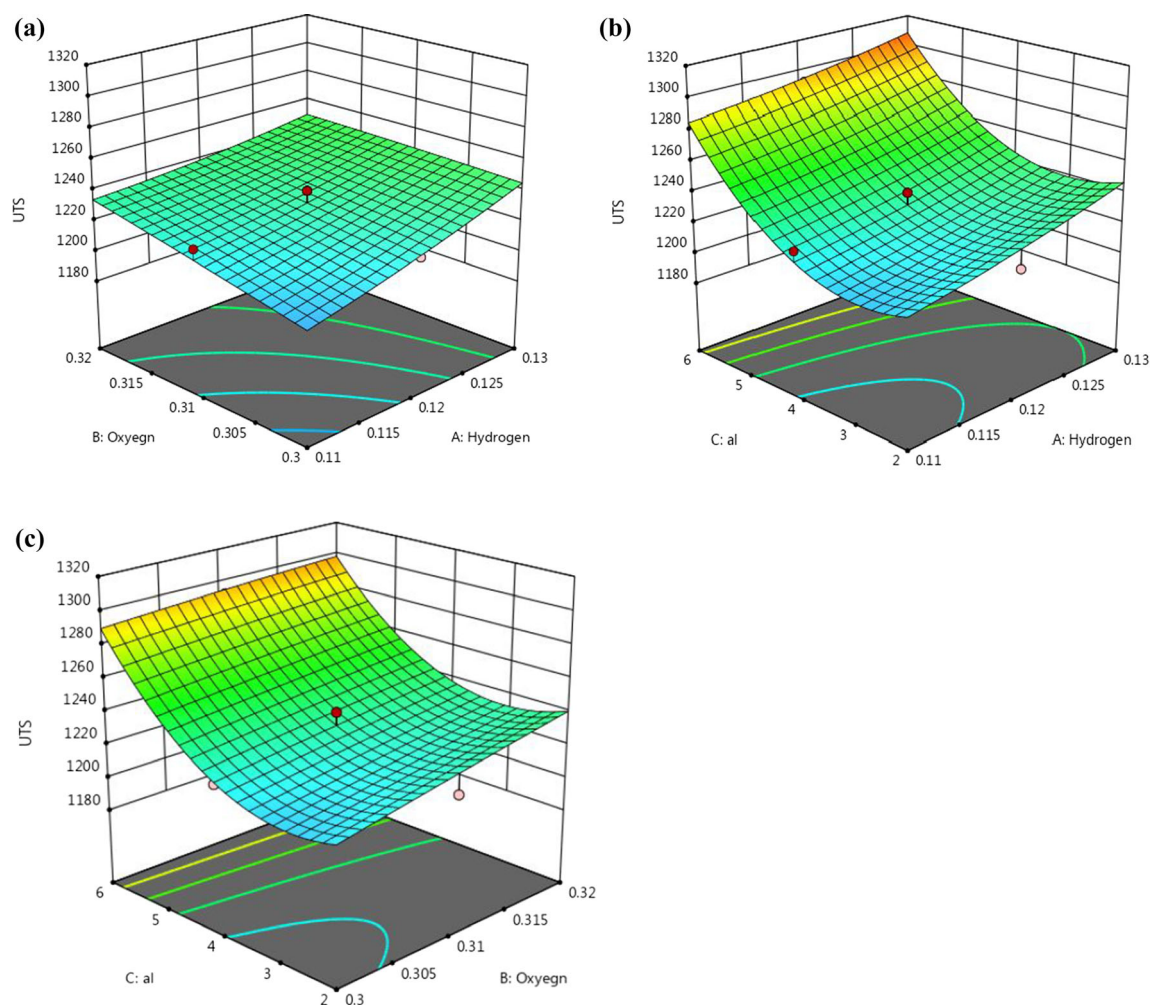


**Figure 3** Interaction between input **a** (oxygen–hydrogen), **b** (aluminum–hydrogen) and **c** (aluminum–oxygen) and output (UTS) parameters.

percentage increases. Aluminum is one of the strongest  $\alpha$  stabilizers, and  $\alpha$  phase has an HCP structure. This structure is generally characterized by low ductility.

### Mechanical properties

The typical tensile stress–strain curves of the tensile test specimens, cut from the extruded rod of the Ti–XAl–2Fe–3Cu alloys, are shown in Figure 6. The average value of ultimate tensile strength (UTS), yield strength (YS) and percentage of elongation to fracture are given in Table 4; for comparison, the data belonging to CP-Ti, Ti–6Al–4V and Ti–5Al–2.5Fe are listed in the table. The UTS, YS and elongation percentage values of the Ti–4Al–2Fe–3Cu alloy were 1230 MPa, 1141 MPa and 2.2%, respectively, while the average UTS, YS and elongation to fracture of the

Ti–2.7Al–2Fe–3Cu alloy were 1220 MPa, 1103 MPa and 2.5%. The results show that the Ti–XAl–2Fe–3Cu alloys possess relatively higher yield and ultimate tensile strengths than CP-Ti, Ti–6Al–4V and Ti–5Al–2.5Fe alloys [31].

### Effect of the microstructure and different phases on mechanical properties

Figure 7 shows the optical microscopy structure of Ti–XAl–2Fe–3Cu with two different aluminum contents. Figure 7 a and b presents a typical microstructure of basket-wave morphology like the other  $\alpha$ + $\beta$  titanium alloys just similar to the commercial Ti–6Al–4V alloy characterized by transformed  $\beta$  phases with lamellar  $\alpha$  phases [32–34].

The Ti–XAl–2Fe–3Cu alloys have a similar microstructure. The core parameters of the lamella



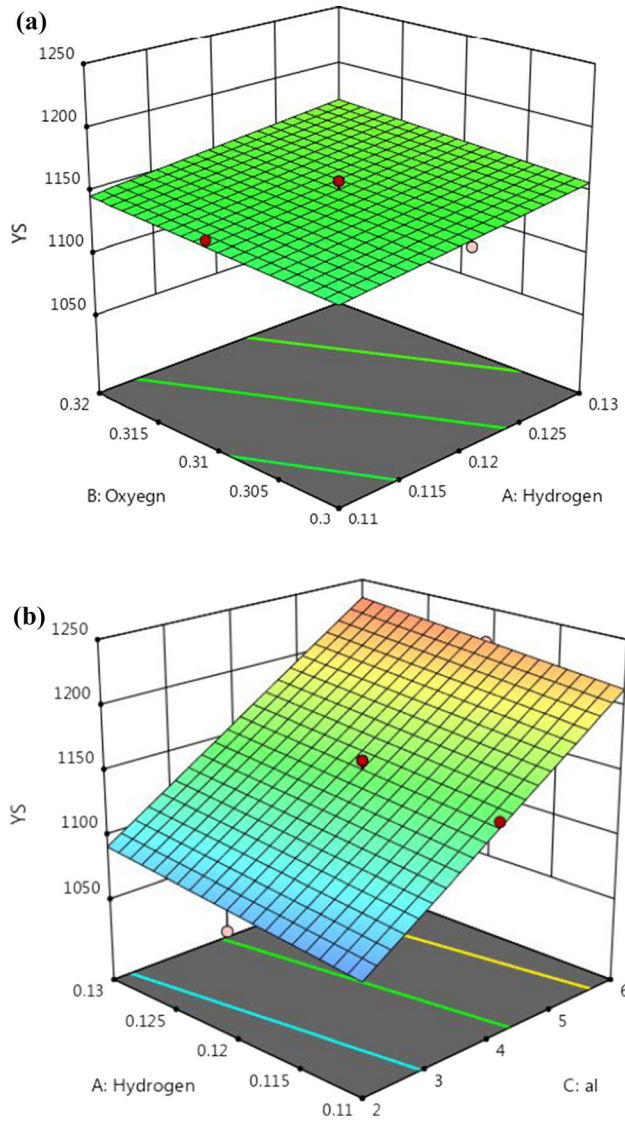


**Figure 4** Interaction between input **a** (oxygen–hydrogen) and **b** (hydrogen–al)) and output (YS) parameters.

structure, with relevant influence on the mechanical properties, are the average size of the cellular grains ( $d_G$ ), lamella thickness ( $\lambda_T$ ) and lamella length ( $\lambda_L$ ) (Fig. 8) [35]. To precisely define the effect of different Al percentage on the morphology of the phases, the size of the  $d_G$ ,  $\lambda_T$  and  $\lambda_L$  in 35 randomly chosen locations of the fabricated Ti–XAl–2Fe–3Cu alloys was analyzed (Fig. 8). The critical parameters in  $\alpha + \beta$  titanium alloys with lamellar structure affecting the mechanical properties are cellular grains, lamella thickness and lamella length. The smaller the sizes of lamella are, the higher the material strength results [31]. The general strengthening mechanisms are related to the grain refinement strengthening,

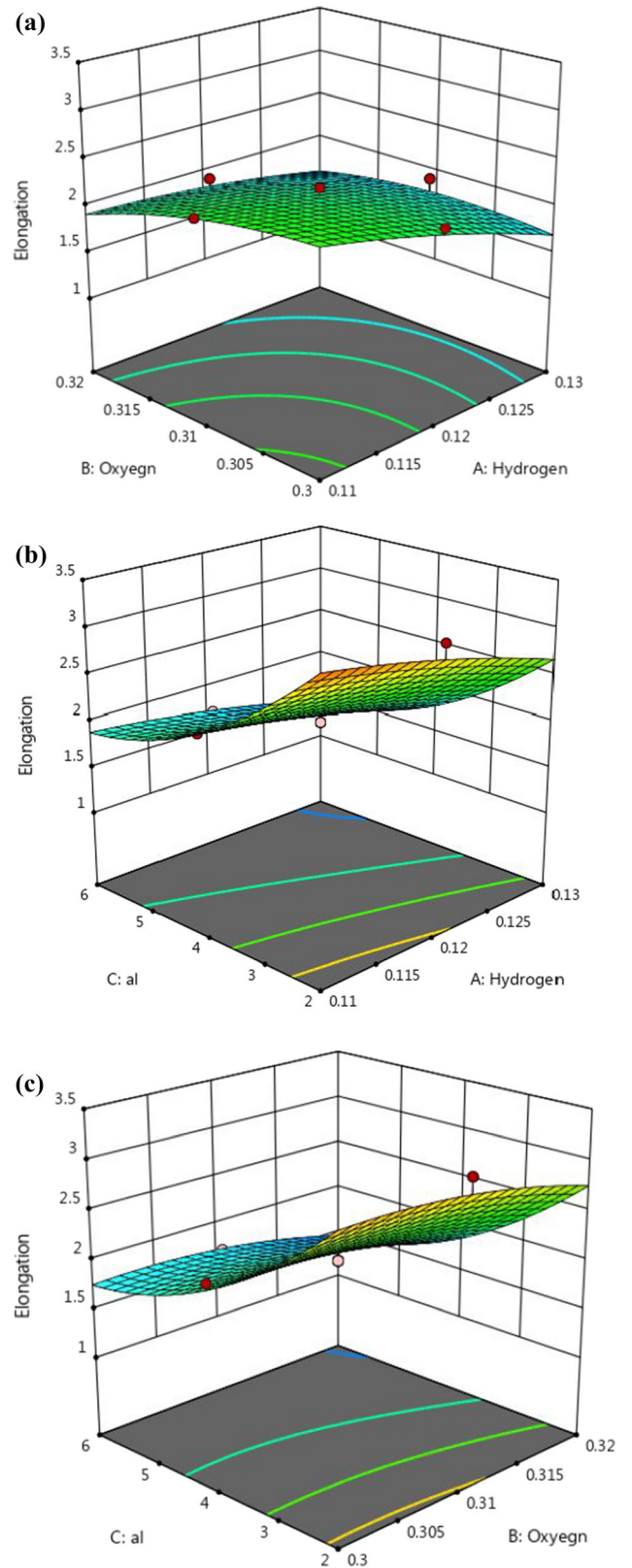


**Figure 5** Interaction between input **a** (oxygen–hydrogen), **b** (aluminum–hydrogen) and **c** (aluminum–oxygen)) and output (elongation) parameters.

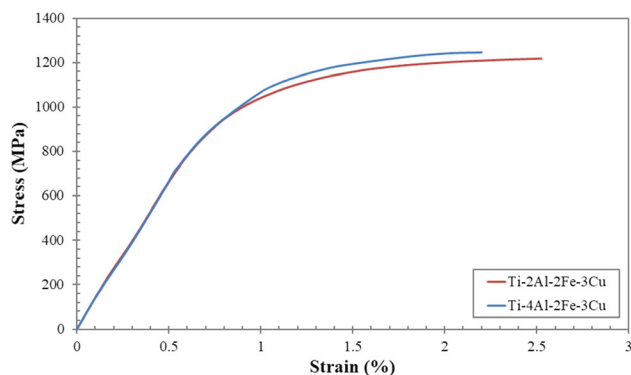


**Figure 6** Engineering stress–strain curves of the Ti–XAl–2Fe–3Cu alloys at room temperature.

**Table 4** Tensile properties of Ti–XAl–2Fe–3Cu alloys compared with the CP-Ti and other alloys

Alloy	YS (MPa)	UTS (MPa)	Elongation (%)
Ti-2Al-2Fe-3Cu	1103	1220	2.5
Ti-4Al-2Fe-3Cu	1141	1230	2.2
CP-Ti	548	649	18.8
Ti-5Al-2.5Fe	820	900	6
Ti-6Al-4 V	895	1000	8

precipitation hardening, solid solution strengthening and dislocation strengthening. So, yield stress can be calculated by Eq. (5) [36]:

$$\sigma_s = \Delta\sigma_{gb} + M(\tau_0 + \Delta\tau_p + \Delta\tau_s + \Delta\tau_d) \quad (5)$$

where  $\sigma_s$  is yield stress,  $\Delta\sigma_{gb}$  is grain refinement strengthening,  $M$  is Taylor factor,  $\tau_0$  is intrinsic critical resolved shear stress,  $\Delta\tau_p$  is precipitation hardening,  $\Delta\tau_s$  is solid solution strengthening, and  $\Delta\tau_d$  is dislocation strengthening, respectively.

The grain refinement strengthening can be calculated by the Hall–Petch relation Eq. (6) [37]:

$$\sigma = \sigma_0 + kd^{-1/2} \quad (6)$$

where  $\sigma$  is yield stress,  $\sigma_0$  is friction stress,  $k$  is Hall–Petch coefficient, and  $d$  is diameter of the grains, but for the current research,  $d$  was considered as average lamella thickness [8].

The lamella thickness in the alloys after heat treatment increases, and according to Eq. (6), the yield strength of the sample decreased.

The average values of these data are shown in Fig. 9. The average sizes of the  $d_G$ ,  $\lambda_T$  and  $\lambda_L$  in the Ti-4Al-2Fe-3Cu alloy were smaller than the Ti-2Al-2Fe-3Cu alloy, respectively.

Figure 10 shows the SEM images of Ti–XAl–2Fe–3Cu specimens with high magnification. The microstructure of the Ti-4Al-2Fe-3Cu has a lamellar  $\alpha$  phase with the grain boundary of  $\alpha$  phase and a trace of precipitation free zones inside the grain; the Ti-2Al-2Fe-3Cu alloy has a typical structure of  $\alpha + \beta$  alloys with the lamellar  $\alpha$  phase and continuous grain boundary of  $\alpha$  phase. The microstructures of Ti-4Al-2Fe-3Cu alloy have some similarity with the Ti-6Al-5Fe-0.05B-0.05C [38] alloy; however, some segments in the structure of Ti-4Al-2Fe-3Cu alloy have a fraction of  $\alpha$  phase, and they have lower ductility. The high strength of the new alloy can be attributed to the fine  $\alpha$  platelets and ultra-fine  $\alpha$ -phase precipitates as shown in Fig. 10a. During the extrusion process, most of the porosity is removed, but, as can be seen in Figs. 10a, b, a small amount of elongated pores are still present.

The EDS point analysis results, in the locations shown in the SEM images in Fig. 10, are listed in Table 5. After extrusion with the Al content of 2 wt.%, the ratio of Fe content in  $\beta$  and  $\alpha$  lamellar was approximately 6.52: 1.16, and increasing the Al content to 4 wt.% caused this ratio to decrease to 5.49: 1.11. On the other hand, almost all Cu atoms stayed in the  $\beta$  lamella and the Cu contents in the  $\alpha$  lamella were below the detection limit of EDS.

The average size of  $\alpha$  lamella and  $\beta$  phases in Ti-4Al-2Fe-3Cu is  $5.2 \pm 1 \mu\text{m}$  and  $7.2 \pm 1.4 \mu\text{m}$ , and the percentage of each phase in Ti-4Al-2Fe-3Cu is 34.51% and 65.49% as presented in Figs. 11 a and b. The average size of  $\alpha$  lamella and  $\beta$  phases in Ti-2Al-2Fe-3Cu is  $8.3 \pm 1.1 \mu\text{m}$  and  $7.6 \pm 1.3 \mu\text{m}$ , and the percentage of each phase in Ti-2Al-2Fe-3Cu is 45.35% and 54.62% as shown in Fig. 11 c and d, respectively. The particle size and percentage of each phase are strongly related to the mechanical properties.

Figure 12 shows the comparison among the XRD patterns of Ti–XAl–2Fe–3Cu alloys. The XRD results of the Ti–XAl–2Fe–3Cu ( $X = 4, 2$  wt %) alloys show that the phase constitution is a combination of both  $\alpha$ -Ti and  $\beta$ -Ti phases. The intermetallic of Ti-Cu was detected, and those intermetallics have similar results as reported by Ren et al. [32] and Zhang et al. [33] for Ti-6Al-4 V-XCu and Ti-Cu alloys, respectively. They mentioned the existence of  $\text{Ti}_2\text{Cu}$  phase, which increased with the increase in the Cu content. The intermetallics correlate with the mechanical property, intermetallics cause increased strength and decreased

**Figure 7** Optical micrographs of the Ti-XAl-2Fe-3Cu alloys: **a** Ti-2Al-2Fe-3Cu and **b** Ti-4Al-2Fe-3Cu.

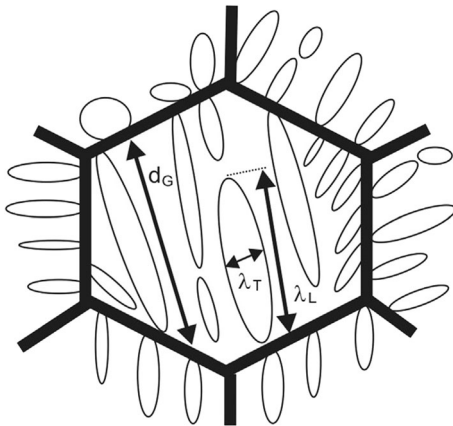
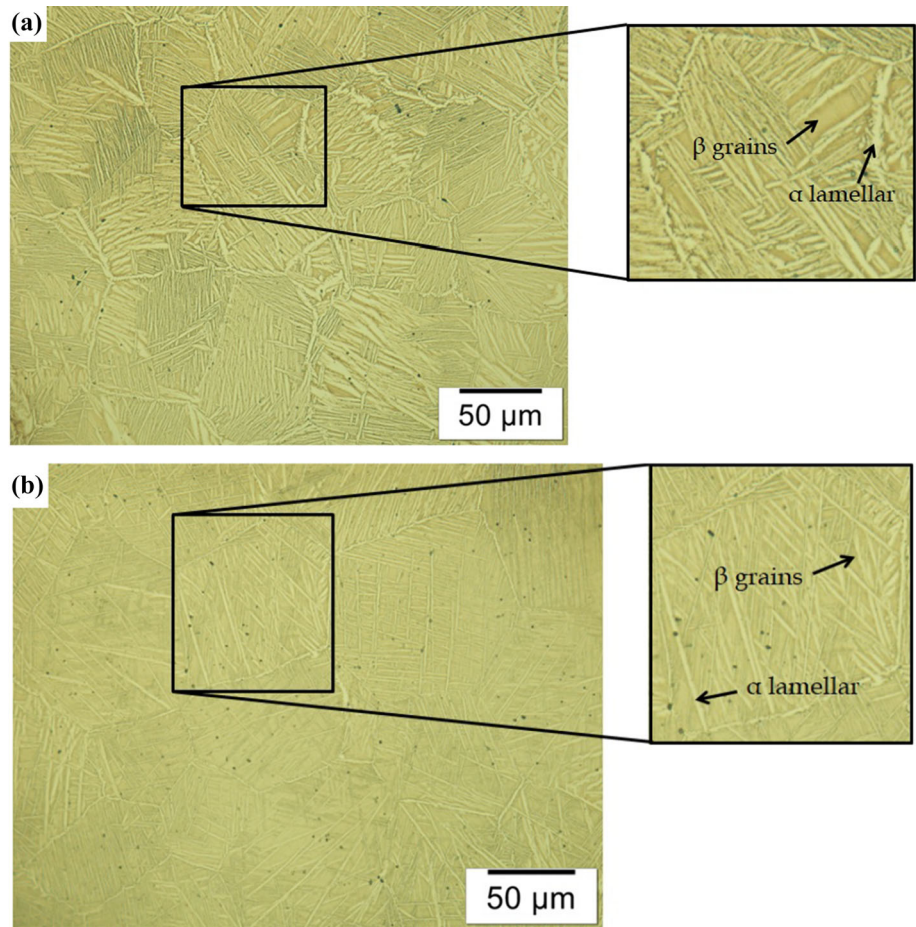


**Figure 8** Schematic diagram of the fully lamellar microstructure of Ti-XAl-2Fe-3Cu alloy:  $d_G$  cellular grains,  $\lambda_T$ -lamellar thickness and  $\lambda_L$ -lamellar length [35].

ductility. This phase is fundamental because its precipitation improves biocorrosion [34, 35, 39–41].

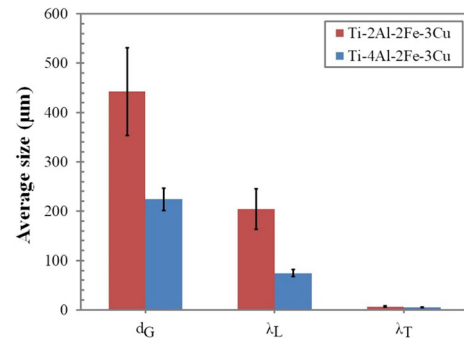


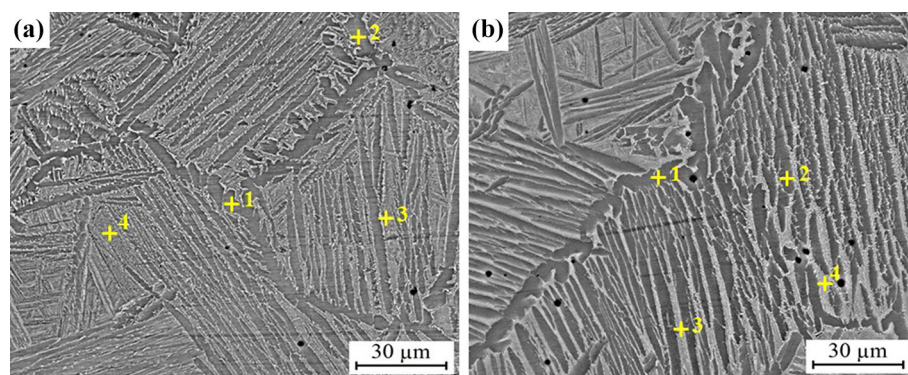
**Figure 9** The average size of the cellular grains ( $d_G$ ), lamellar length ( $\lambda_L$ ) and lamellar thickness ( $\lambda_T$ ) of the Ti-XAl-2Fe-3Cu alloys.

### Effect of the oxygen and hydrogen content on mechanical properties and fracture behavior

The oxygen and hydrogen contents have a direct connection with the mechanical properties. Based on Table 1, the oxygen content of the Ti-4Al-2Fe-3Cu rod was 0.3 wt%, the oxygen content of the



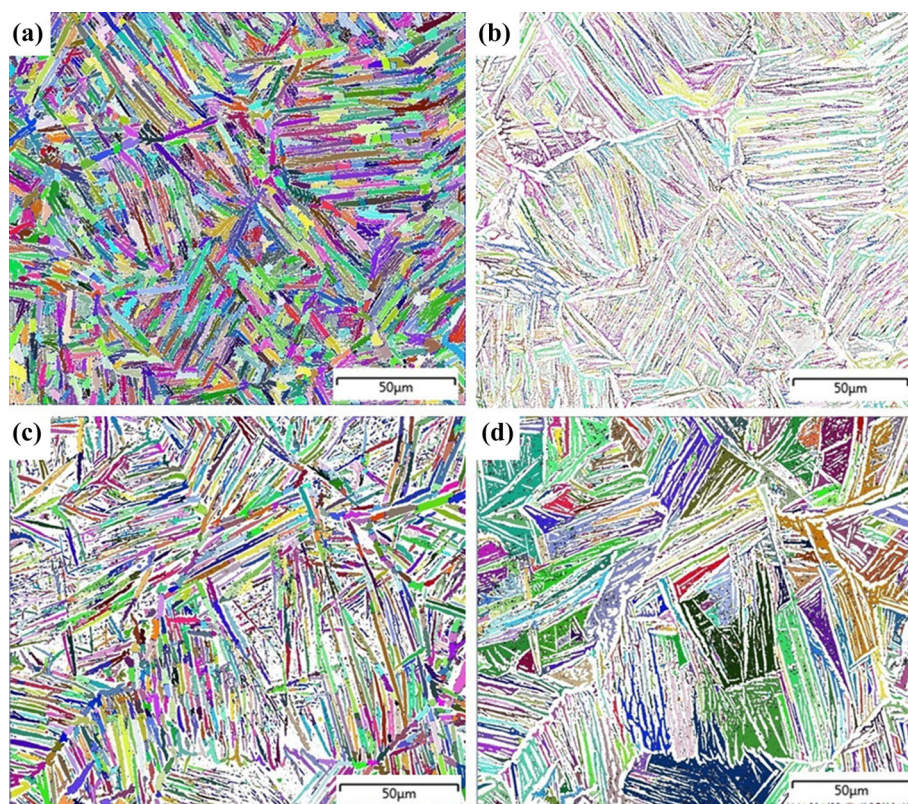
**Figure 10** SEM micrographs of Ti-XAl-2Fe-3Cu alloys: **a** Ti-2Al-2Fe-3Cu; **b** Ti-4Al-2Fe-3Cu.



**Table 5** EDS analysis results of the as-extruded sample of Ti-XAl-2Fe-3Cu alloys

Alloy	Location	Composition (wt.%)				Possible phase
		Ti	Al	Fe	Cu	
Ti-4Al-2Fe-3Cu	1	94.31	4.58	1.11	–	$\alpha$ -Ti
	2	94.28	4.69	1.03	–	$\alpha$ -Ti
	3	84.46	3.03	5.27	7.24	$\beta$ -Ti
	4	85.38	3.08	5.49	6.05	$\beta$ -Ti
Ti-2Al-2Fe-3Cu	1	95.6	3.24	1.16	–	$\alpha$ -Ti
	2	95.85	3.05	1.1	–	$\alpha$ -Ti
	3	85.32	1.85	6.2	6.63	$\beta$ -Ti
	4	85.59	2.12	6.52	5.77	$\beta$ -Ti

**Figure 11** Shows the aggregation of  $\alpha$  lamellar and  $\beta$  phases in Ti-XAl-2Fe-3Cu: **a**  $\alpha$  lamellar in Ti-2Al-2Fe-3Cu; **b**  $\beta$  in Ti-2Al-2Fe-3Cu; **c**  $\alpha$  lamellar in Ti-4Al-2Fe-3Cu; **d**  $\beta$  in Ti-4Al-2Fe-3Cu.



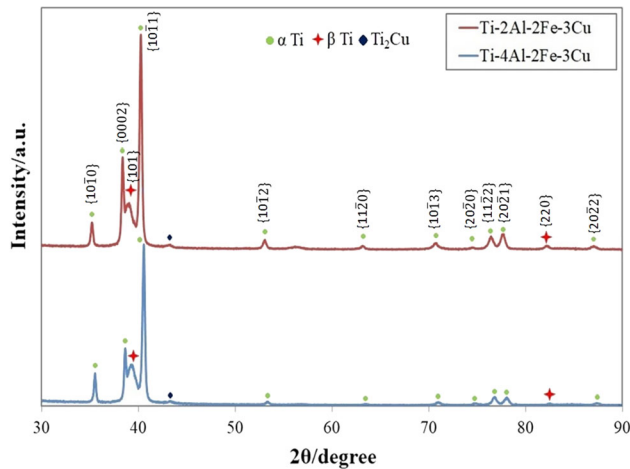


**Figure 12** XRD patterns of the Ti-XAl-2Fe-3Cu alloys.

Ti-2Al-2Fe-3Cu rod was 0.32 wt%, the hydrogen content of the Ti-4Al-2Fe-3Cu rod was 0.12 wt%, and the hydrogen content of the Ti-2Al-2Fe-3Cu rod was 0.13 wt%. Therefore, the oxygen content in rods was almost constant, but the hydrogen content in the samples is higher than standard. Hydrogen content makes Ti-2Fe-3Cu-XAl ( $X = 4-2.7$ ) alloys brittle [31]. The hydrogen content in these alloys is higher than the standard of commercial titanium alloys value. This high percentage is the reason for the low ductility [31].

Figure 13 shows the fracture surfaces of Ti-4Al-2Fe-3Cu and Ti-2Al-2Fe-3Cu specimens, respectively. As can be seen in Fig. 13a, Ti-4Al-2Fe-3Cu alloy shows a combination of transgranular or brittle cleavage facets, the fracture surface presents the massive part of a cleavage structure with few microporous and dimples. Figure 13b represents the fracture surface of Ti-2Al-2Fe-3Cu. As can be seen, it has a structure similar to the Ti-4Al-2Fe-3Cu, but with more dimples and small micropores. The fracture surface of both alloys is related to the mechanical properties, demonstrating that the Ti-2Al-2Fe-3Cu is more ductile.

### Biocorrosion properties

Electrochemical impedance tests, carried out open-circuit potential ( $E_{ocp}$ ) after 1 h immersion, are shown in Fig. 14a. The Nyquist plot (Fig. 14a) for different values of Al in Ringer’s solution showed similar behavior which reported by other researchers for Ti alloys [42, 43]. It can be seen that the diameters of Nyquist curves of the Ti-4Al-2Fe-3Cu alloys are

larger in comparison with Ti-2Al-2Fe-3Cu sample which indicates improvement on corrosion resistance. The EIS results were fitted by an equivalent circuit used in previous studies [44–46]. It showed that, by increasing aluminum content from 2 to 4%, the polarization resistance values increase from about 230  $K\Omega cm^2$  to about 280  $K\Omega cm^2$ . Figure 14b compares the polarization curves of the titanium samples in Ringer’s solution. The corrosion current density estimated from these curves was 0.158  $\mu A/cm^2$  for the Ti-2Al-2Fe-3Cu and 0.131  $\mu A/cm^2$  for Ti-4Al-2Fe-3Cu sample. Furthermore, a clear decrease in passive current density with the increase in the Al content can be observed in all Ti- XAl-2Fe-3Cu alloys. This can be linked to the low-defects oxide layer on Ti-4Al-2Fe-3Cu alloy surface due to the addition of Al.

### Effect of process parameters on $I_{corr}$

From Fig. 15, it can be observed that the corrosion current density ( $I_{corr}$ ) forms the polarization parameters in Ringer’s solution changing with the alloying elements. Aluminum contents have a strong effect on the corrosion resistivity of the alloys. By increasing Al content,  $I_{corr}$  is extremely reduced. The increase in corrosion current density reduces the corrosion resistivity. The total amount of ions released for Ti-4Al-3Fe-3Cu alloy in Ringer’s solution is lower if compared to Ti-2Al-2Fe-3Cu, hence signifying the lower toxicity of the Ti-4Al-3Fe-3Cu alloy. This can be linked to the low-defects diffusionless oxide layer on the high percentage of Al content surface due to the addition of Al. The Ti-Fe alloys have higher corrosion resistance in Hank’s solution than the CP-Ti [47]. Based on the literature, stability of the passive film is improved through the addition of iron [48].

To run optimization, the range of the parameters is firstly determined. In the current research, range of used parameters was given in Table 6. To run the optimization, each parameter must have the importance and weight based on the project’s requirements.

When the target is to find maximum [49]:

$$d_i = \begin{cases} 0 & Y_i < Low_i \\ \left( \frac{Y_i - Low_i}{High_i - Low_i} \right)^w & Low_i < Y_i < High_i \\ 1 & Y_i > High_i \end{cases} \quad (7)$$

When the target is to find minimum [49]:



**Figure 13** SEM micrograph of fractured surfaces of Ti–XAl–2Fe–3Cu alloys: **a** Ti–2Al–2Fe–3Cu, **b** Ti–4Al–2Fe–3Cu.

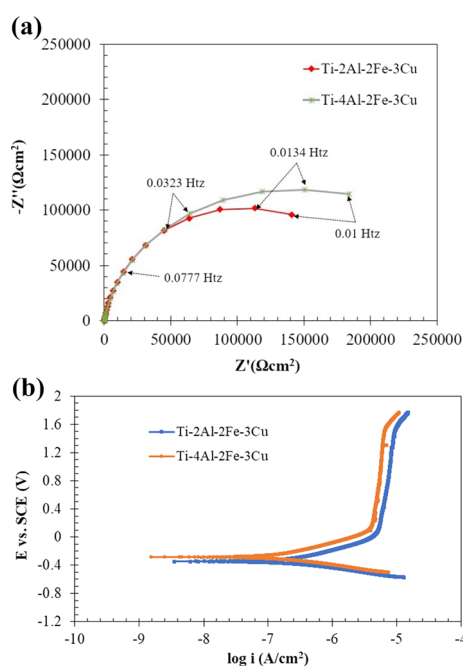
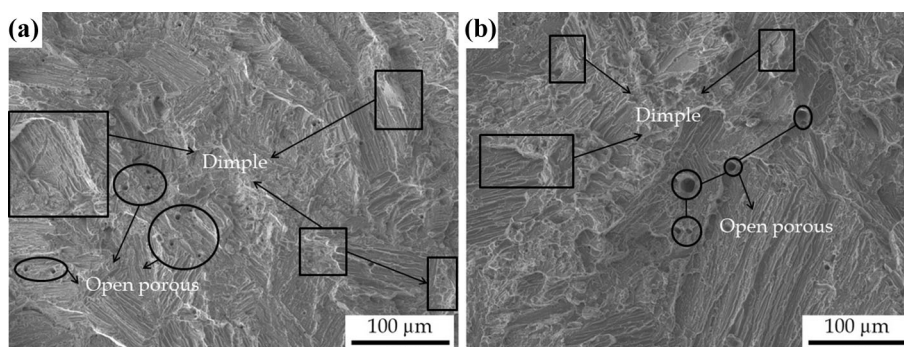


**Figure 14** **a** The Nyquist diagrams of Ti–XAl–2Fe–3Cu samples after 1-h immersion in the Ringer’s solution, **b** Polarization curves of the Ti–XAl–2Fe–3Cu samples in the Ringers’ solution.

$$d_i = \begin{cases} 1 & Y_i < \text{Low}_i \\ \left( \frac{Y_i - \text{Low}_i}{\text{High}_i - \text{Low}_i} \right)^{w_i} & \text{Low}_i < Y_i < \text{High}_i \\ 0 & Y_i > \text{High}_i \end{cases} \quad (8)$$

$$D = \left( \prod_{i=1}^n d_i^{r_i} \right)^{1/\sum r_i} \quad (9)$$

The “ $d_i$ ,” “ $w_i$ ,” “ $D$ ” and “ $r$ ” show the unique desirability of each response, weight field, desirability objective function and importance.

Once processed the data through the software, the optimal combination is extracted as shown in Table 7 and to check the accuracy of achieved results, a confirmatory test must be done.

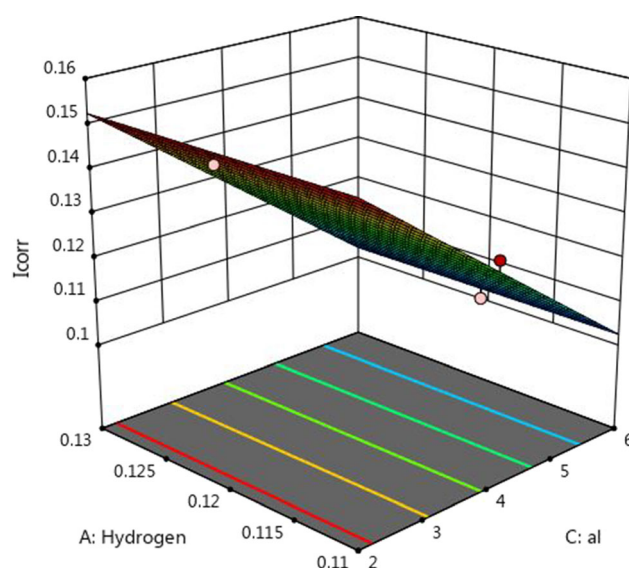


**Figure 15** Interaction between input (hydrogen–al) and output ( $I_{\text{corr}}$ ) parameters.

In Table 8, it can be seen that the achieved results are in the good correlation based on the project requirements.

## Conclusions

In the present research, it was tried to optimize the process parameters of Ti–XAl–2Fe–3Cu powder compact extrusion via RSM and experimental tests. Having done the microstructural analysis, the  $\alpha/\beta$  lamellar structure was observed. Based on the achieved results, the size and morphology of the coarse plate-like  $\alpha$  phase varied increasing aluminum content, and  $\alpha$  structure became finer with the increase in the Al content. By enhancing the Al content, the YS of the Ti–XAl–2Fe–3Cu alloy increases, but its ductility slightly decreases. The key reason that supports this phenomenon is the amount of  $\beta$

**Table 6** Weight and importance of parameters

Name	Goal	Lower limit	Upper limit	Lower weight	Upper weight	Importance
Hydrogen	Is in range	0.11	0.13	1	1	3
Aluminum	Is in range	2	6	1	1	3
Oxygen	Is in range	0.3	0.32	1	1	3
Elongation	Minimize	1.2	3.5	1	1	3
UTS	Maximize	1185	1320	1	1	5
YS	Maximize	1052	1245	1	1	3
$I_{\text{corr}}$	Maximize	0.1	0.15	1	1	3

**Table 7** Desired parameters

No	Hydrogen	Oxygen	Al	Elongation	UTS	YS	$I_{\text{corr}}$	Desirability	
1	0.130	0.319	6.000	1.295	1306.094	1240.719	0.103	0.938	Selected

**Table 8** Confirmatory tests

Performance	Units	Desirability function	Experiment
Elongation	%	1.295	1.2
UTS	MPa	1306.094	1320
YS	MPa	1240.719	1245
$I_{\text{corr}}$	$\mu\text{A}/\text{cm}^2$	0.103	0.1

phase. The highest percentage of oxygen and hydrogen content in Ti-XAl-2Fe-3Cu alloys reduces the ductility through the induction of a brittle cleavage structure appearing on the fracture surface. The corrosion resistivity of the Ti alloys is increased with the increase in the Al percentage. Also, oxygen and hydrogen do not have any crucial effect on the corrosion resistivity of Ti alloys [50].

### Date availability

The data from this study are available from the corresponding author upon reasonable request.

### Funding

Open access funding provided by Università del Salento within the CRUI-CARE Agreement.

### Declarations

**Conflict of interest** The authors declare that they have no known competing financial interests or personal relationships that could have appeared to influence the work reported in this paper.

**Open Access** This article is licensed under a Creative Commons Attribution 4.0 International License, which permits use, sharing, adaptation, distribution and reproduction in any medium or format, as long as you give appropriate credit to the original author(s) and the source, provide a link to the Creative Commons licence, and indicate if changes were made. The images or other third party material in this article are included in the article's Creative Commons licence, unless indicated otherwise in a credit line to the material. If material is not included in the article's Creative Commons licence and your intended use is not permitted by statutory regulation or exceeds the permitted use, you will need to obtain permission directly from the copyright holder. To view a copy of this licence, visit <http://creativecommons.org/licenses/by/4.0/>.

### References

- [1] Leyens C, Peters M (2003) Titanium and titanium alloys. Wiley-VCH, Weinheim, Germany
- [2] Shan DB, Yang GP, Xu WC (2009) Deformation history and the resultant microstructure and texture in backward tube spinning of Ti-6Al-2Zr-1Mo-1V. J Mater Process Technol

- 209:5713–5719. <https://doi.org/10.1016/j.jmatprotec.2009.05.034>
- [3] Atapour M, Al P, Frankel GS, Williams JC (2011) Corrosion behavior of  $\beta$  titanium alloys for biomedical applications. *Mater Sci Eng C* 31:885–891. <https://doi.org/10.1016/j.msec.2011.02.005>
- [4] Arrazola PJ, Garay A, Iriarte LM, Armendia M, Marya S, Le Maître F (2009) Machinability of titanium alloys (Ti6Al4V and Ti555.3). *J Mater Process Technol* 209:2223–2230. <https://doi.org/10.1016/j.jmatprotec.2008.06.020>
- [5] Geetha M, Mudali UK, Gogia AK, Asokamani R, Raj B (2004) Influence of microstructure and alloying elements on corrosion behavior of Ti–13Nb–13Zr alloy. *Corros Sci* 46:877–892. [https://doi.org/10.1016/S0010-938X\(03\)00186-0](https://doi.org/10.1016/S0010-938X(03)00186-0)
- [6] Chirico C, Vaz Romero A, Gordo E, Tsipas SA (2022) Improvement of wear resistance of low-cost powder metallurgy  $\beta$ -titanium alloys for biomedical applications. *Surf Coat Technol* 434:128207. <https://doi.org/10.1016/j.surfcoat.2022.128207>
- [7] Oliveira NTC, Aleixo G, Caram R, Guastaldi AC (2007) Development of Ti–Mo alloys for biomedical applications: microstructure and electrochemical characterization. *Mater Sci Eng A* 452:727–731. <https://doi.org/10.1016/j.msea.2006.11.061>
- [8] Najafzadeh M, Bahadoran A, Bozorg M, Sadeghi B, Liang J, Zhang D (2021) Microstructures and mechanical properties of high strength Ti–XAl–2Fe–3Cu alloys fabricated by powder compact extrusion. *J Alloys Compd* 884:161136. <https://doi.org/10.1016/j.jallcom.2021.161136>
- [9] Najafzadeh M, Bozorg M, Bahadoran A, Liang J, Zhang D (2021) Compressive and biocorrosion properties of Ti–XAl–2Fe–3Cu alloys fabricated by powder metallurgy. *J Alloys Compd* 884:161079. <https://doi.org/10.1016/j.jallcom.2021.161079>
- [10] Shah R, Gashi B, Hoque S, Marian M, Rosenkranz A (2021) Enhancing mechanical and biomedical properties of prostheses—Surface and material design. *Surf Interfaces* 27:101498. <https://doi.org/10.1016/j.surfim.2021.101498>
- [11] Aniołek K, Łosiewicz B, Kubisztal J, Osak P, Stróż A, Barylski A, Kaptacz S (2021) Mechanical properties, corrosion resistance and bioactivity of oxide layers formed by isothermal oxidation of Ti–6Al–7Nb alloy. *Coatings* 11:505. <https://doi.org/10.3390/coatings11050505>
- [12] Guan J, Jiang X, Xiang Q, Yang F, Liu J (2021) Corrosion and tribocorrosion behavior of titanium surfaces designed by electromagnetic induction nitriding for biomedical applications. *Surf Coat Technol* 409:126844. <https://doi.org/10.1016/j.surfcoat.2021.126844>
- [13] Park YJ, Song YH, An JH, Song HJ, Anusavice KJ (2013) Cytocompatibility of pure metals and experimental binary titanium alloys for implant materials. *J Dent* 41:1251–1258. <https://doi.org/10.1016/j.jdent.2013.09.003>
- [14] Mareci D, Rusu I, Chelariu R, Bolat G, Munteanu C, Suti-man D, Souto RM (2013) Application of dynamic electrochemical impedance spectroscopy to the evaluation of the corrosion resistance of a historic bronze object in artificial acid rainwater. *Eur J Sci Theol* 9:189–199
- [15] Zhou YL, Luo DM (2011) Corrosion behavior of Ti–Mo alloys cold-rolled and heat treated. *J Alloys Compd* 509:6267–6272. <https://doi.org/10.1016/j.jallcom.2011.03.045>
- [16] Buenconsejo PJS, Kim HY, Miyazaki SC (2009) Effect of ternary alloying elements on the shape memory behavior of Ti–Ta alloys. *Acta Mater* 57:2509–2515. <https://doi.org/10.1016/j.actamat.2009.02.007>
- [17] Niu J, Guo Y, Li K, Liu W, Dan Z, Sun Z, Chang H (2021) Improved mechanical, bio-corrosion properties and in vitro cell responses of Ti–Fe alloys as candidate dental implants. *Mater Sci Eng C* 122:111917. <https://doi.org/10.1016/j.msec.2021.111917>
- [18] Vincent M, Hartemann P, Engels-Deutsch M (2016) Antimicrobial applications of copper. *Int J Hygiene Environ Health* 219:585–591. <https://doi.org/10.1016/j.ijheh.2016.06.003>
- [19] Shirai T, Tsuchiya H, Shimizu T, Ohtani K, Zen Y, Tomita K (2009) Prevention of pin tract infection with titanium–copper alloys. *J Biomed Mater Res A* 91:373–380. <https://doi.org/10.1002/jbm.b.31412>
- [20] Najafzadeh M, Zhang D, Maldar A, Bozorg M, Liang J (2022) Microstructure and mechanical properties of a high-strength Ti–4Al–2Fe–3Cu alloy fabricated by sintering and hot extrusion. *Metall Mater Trans A* 53:1955–1968. <https://doi.org/10.1007/s11661-022-06668-4>
- [21] Najafzadeh M, Ghasempour-Mouziraji M (2021) Multi-objective optimization of process parameters in pack siliconizing on AISI D2 steel. *SILICON* 13:2233–2242. <https://doi.org/10.1007/s12633-020-00735-4>
- [22] Hosseinzadeh M, Mehran Ghasempour M (2016) An analysis of tube drawing process used to produce squared sections from round tubes through FE simulation and response surface methodology. *Int J Adv Manuf Technol* 87(5):2179–2194. <https://doi.org/10.1007/s00170-016-8532-5>
- [23] Lv B, Wang S, Xu T, Guo F (2021) Effects of minor Nd and Er additions on the precipitation evolution and dynamic recrystallization behavior of Mg–6.0Zn–0.5Mn alloy. *J Magnes Alloys* 9(3):840–852. <https://doi.org/10.1016/j.jm.a.2020.06.018>

- [24] Huang Y, An C, Zhang Q, Zang L, Shao H, Liu, Y,... Wang, Y. (2021) Cost-effective mechanochemical synthesis of highly dispersed supported transition metal catalysts for hydrogen storage. *Nano Energy* 80:105535. <https://doi.org/10.1016/j.nanoen.2020.105535>
- [25] Zhang X, Tang Y, Zhang F, Lee C (2016) A novel aluminum-graphite dual-ion battery. *Adv Energy Mater* 6(11):1502588. <https://doi.org/10.1002/aenm.201502588>
- [26] Liu W, Li J, Zheng J, Song Y, Shi Z, Lin, Z,... Chai, L. (2020) Different pathways for Cr(III) oxidation: implications for Cr(VI) reoccurrence in reduced chromite ore processing residue. *Environ Sci Technol* 54(19):11971–11979. <https://doi.org/10.1021/acs.est.0c01855>
- [27] Liu W, Guo Z, Wang C, Niu S (2021) Physico-mechanical and microstructure properties of cemented coal Gangue-Fly ash backfill: effects of curing temperature. *Constr Build Mater* 299:124011. <https://doi.org/10.1016/j.conbuildmat.2021.124011>
- [28] Xie Y, Meng X, Wang F, Jiang Y, MaWan XL, Huang Y (2021) Insight on corrosion behavior of friction stir welded AA2219/AA2195 joints in astronautical engineering. *Corros Sci* 192:109800. <https://doi.org/10.1016/j.corsci.2021.109800>
- [29] Zhou K, Xu J, Xiao G, Huang Y (2022) A novel low-damage and low-abrasive wear processing method of Cf/SiC ceramic matrix composites: laser-induced ablation-assisted grinding. *J Mater Process Technol.* <https://doi.org/10.1016/j.jmatprotec.2022.117503>
- [30] Rahimi-Golkhandana M, Danesha S, Davoodib A (2021) Effects of temperature and changing disinfectants on steel water pipes corrosion: case study of Mashhad Iran. *Water Conserv Manag* 2(5):47–53. <https://doi.org/10.26480/wcm.02.2021.47.53>
- [31] Lütjering G, Williams JC (2007) *Titanium*, 2nd edn. Springer, Berlin Heidelberg
- [32] Ren L, Ma Z, Li M, Zhang Y, Liu W, Liao Z, Yang K (2014) Antibacterial properties of Ti–6Al–4V–xCu alloys. *J Mater Sci Technol* 30:699–705. <https://doi.org/10.1016/j.jmst.2013.12.014>
- [33] Zhang E, Li F, Wang H, Liu J, Wang C, LiMand Yang K (2013) A new antibacterial titanium–copper sintered alloy: preparation and antibacterial property. *Mater Sci Eng C* 33:4280–4287. <https://doi.org/10.1016/j.msec.2013.06.016>
- [34] Alshammari Y, Yang F, Bolzoni L (2019) Low-cost powder metallurgy Ti-Cu alloys as a potential antibacterial material. *J Mech Behav Biomed Mater* 95:232–239. <https://doi.org/10.1016/j.jmbbm.2019.04.004>
- [35] Tsao LC (2017) Effects of Cu addition on the microstructure and mechanical properties of Ti15Sn alloys. *Mater Sci Eng A* 698:98–103. <https://doi.org/10.1016/j.msea.2017.05.046>
- [36] Du YZ, Zheng MY, Qiao XG, Wang DB, Peng WQ, Wu K, Jiang BL (2016) Improving microstructure and mechanical properties in Mg–6 mass% Zn alloys by combined addition of Ca and Ce. *Mater Sci Eng A* 656:67–74. <https://doi.org/10.1016/j.msea.2016.01.034>
- [37] Yan H, Gong X, Chen J, Cheng M (2021) Microstructure, texture characteristics, mechanical and bio-corrosion properties of high strain rate rolled Mg–Zn–Sr alloys. *Met Mater Int* 27:2249–2263. <https://doi.org/10.1007/s12540-019-00601-y>
- [38] Liang Z, Miao J, Brown T, Sachdev AK, Williams JC, Luo AA (2018) A low-cost and high-strength Ti-Al-Fe-based cast titanium alloy for structural applications. *Scripta Mater* 157:124–128. <https://doi.org/10.1016/j.scriptamat.2018.08.005>
- [39] Wang X, Zhang LJ, Ning J, Na SJ (2022) Effect of Cu-induced eutectoid transformation on microstructure and mechanical properties of Ti–6Al–4V alloy by laser wire deposition. *Mater Sci Eng A* 833:142316. <https://doi.org/10.1016/j.msea.2021.142316>
- [40] Xu D, Wang T, Lu Z, Wang Y, Sun B, Wang S (2021) Ti–6Al–4V–5Cu synthesized for antibacterial effect in vitro and in vivo via contact sterilization. *J Mater Sci Technol* 90:133–142. <https://doi.org/10.1016/j.jmst.2021.03.007>
- [41] Yao X, Sun QY, Xiao L, Sun J (2009) Effect of Ti<sub>2</sub>Cu precipitates on mechanical behavior of Ti–2.5Cu alloy subjected to different heat treatments. *J Alloys Compd* 484:196–202. <https://doi.org/10.1016/j.jallcom.2009.04.095>
- [42] Mohammadtaheri M, Bozorg M, Yazdani A, Salehi M (2022) Fabrication of Ti–Al<sub>2</sub>O<sub>3</sub>–HA composites by spark plasma sintering and its properties for medical applications. *J Mater Res.* <https://doi.org/10.1557/s43578-022-00561-x>
- [43] Fattah-alhosseini A, Reza A, Mazaheri Y, Keshavarz MK (2016) Effect of immersion time on the passive and electrochemical response of annealed and nano-grained commercial pure titanium in Ringer’s physiological solution at 37 °C. *Mater Sci Eng C* 71:771–779. <https://doi.org/10.1016/j.msec.2016.10.057>
- [44] Izquierdo J, González-marrero MB, Bozorg M, Fernández-pérez BM (2016) Multiscale electrochemical analysis of the corrosion of titanium and nitinol for implant applications. *Electrochim Acta* 203:366–378. <https://doi.org/10.1016/j.electacta.2016.01.146>
- [45] De Assis SL, Wolyneć S, Costa I (2006) Corrosion characterization of titanium alloys by electrochemical techniques. *Electrochim Acta* 51:1815–1819. <https://doi.org/10.1016/j.electacta.2005.02.121>
- [46] Pan C, Wang X, Behnamian Y, Zhong Wu, Qin Z, Xia D-H, Wenbin Hu (2020) Monododecyl phosphate film on LY12 aluminum alloy: pH-controlled self-assembly and corrosion

- resistance. *J Electrochem Soc* 167:161510. <https://doi.org/10.1149/1945-7111/abd3bb>
- [47] Niu J, Guo Y, Li K, Liu W, Dan Z, Sun Z, Chang H, Zhou L (2021) Improved mechanical, bio-corrosion properties and in vitro cell responses of Ti-Fe alloys as candidate dental implants. *Mater Sci Eng C* 122:111917. <https://doi.org/10.1016/j.msec.2021.111917>
- [48] Lu J, Zhao Y, Niu H, Zhang Y, Du Y, Zhang W, Huo W (2016) Electrochemical corrosion behavior and elasticity properties of Ti-6Al-xFe alloys for biomedical applications. *Mater Sci Eng C* 62:36–44. <https://doi.org/10.1016/j.msec.2016.01.019>
- [49] Najafizadeh M, Hossainzadeh M, Ghasempour-Mouziraji M, Perrone A, Cavaliere P (2022) Pack siliconizing optimization of AISI D2 tool steel. *Silicon*. <https://doi.org/10.1007/s12633-022-01760-1>
- [50] Rai PK, Naidu D, Vajpai SK et al (2021) Effect of cold rolling and heat treatment on corrosion and wear behavior of  $\beta$ -titanium Ti-25Nb-25Zr Alloy. *J Mater Eng Perform* 30:4174–4182. <https://doi.org/10.1007/s11665-021-05739-8>

**Publisher's Note** Springer Nature remains neutral with regard to jurisdictional claims in published maps and institutional affiliations.

